Comparison of Kinetic and Equilibrium Reaction Models in Simulating Gas Hydrate Behavior in Porous Media

Michael B. Kowalsky * and George J. Moridis

Earth Sciences Division, Lawrence Berkeley National Laboratory, 1 Cyclotron Road, M.S. 90-1116, Berkeley, CA, 94720, USA

Abstract

In this study we compare the use of kinetic and equilibrium reaction models in the simulation of gas (methane) hydrate behavior in porous media. Our objective is to evaluate through numerical simulation the importance of employing kinetic versus equilibrium reaction models for predicting the response of hydrate-bearing systems to external stimuli, such as changes in pressure and temperature. Specifically, we (1) analyze and compare the responses simulated using both reaction models for natural gas production from hydrates in various settings and for the case of depressurization in a hydrate-bearing core during extraction; and (2) examine the sensitivity to factors such as initial hydrate saturation, hydrate reaction surface area, and numerical discretization. We find that for large-scale systems undergoing thermal stimulation and depressurization, the calculated responses for both reaction models are remarkably similar, though some differences are observed at early times. However, for modeling short-term processes, such as the rapid recovery of a hydrate-bearing core, kinetic limitations can be important, and neglecting them may lead to significant under-prediction of recoverable hydrate. The use of the equilibrium reaction model often appears to be justified and preferred for simulating the behavior of gas hydrates, given that the computational demands for the kinetic reaction model far exceed those for the equilibrium reaction model.

Keywords: Gas hydrates; Dissociation; Kinetics; Depressurization; Thermal stimulation; Core recovery.

* Corresponding author. Tel.: +1 510 486 7314; fax: +1 510 486 5686.
E-mail address: MBKowalsky@lbl.gov (M. B. Kowalsky).

1. Introduction

1.1. Background

Gas hydrates are solid crystalline compounds in which gas molecules (referred to as guests) are lodged within the lattices of ice crystals (called hosts). Under suitable conditions of low temperature and high pressure, a gas G will react with water to form hydrates according to

$$G\ (g) + N_H H_2O\ (w) = G \cdot N_H H_2O\ (h), \tag{1}$$

where N_H is the hydration number and *g, w,* and *h* refer to gas, water, and hydrate, respectively. Of particular interest are methane hydrates ($G = CH_4$), which represent the majority of natural gas hydrates.

The amount of hydrocarbons residing in hydrate deposits is estimated to substantially exceed all known conventional oil and gas resources [1, 2, 3]. Such deposits occur in two distinct geologic settings where the necessary low temperatures and high pressures exist for their formation and stability: beneath the permafrost and in ocean sediments.

Because of the sheer size of the resource and the ever-increasing energy demand, hydrocarbon hydrates are attracting increasing attention as a potential alternative energy resource [4, 5]. With hydrates being strong cementing agents, the geomechanical behavior of hydrate-bearing sediments in response to thermal and mechanical stresses (natural or anthropogenic) is of particular importance in marine systems because it may lead to deteriorating structural integrity of the oceanic sediment formations that support structures such as hydrocarbon production platforms [6, 7, 8]. There is also evidence linking the large-scale behavior of gas hydrates to instances of rapid global warming in the geologic past [9, 10]. The scientific and economic implications of all these issues have necessitated

the development and evaluation of models that can accurately predict the behavior of gas hydrates in porous media.

As *Makogon* [11] indicated, the three main methods of hydrate dissociation are (1) depressurization, in which the pressure P is lowered below the equilibrium pressure P_e for hydrate formation at the prevailing temperature T; (2) thermal stimulation, in which T is raised above the equilibrium temperature T_e for hydrate formation at the prevailing P; and (3) through the use of inhibitors (such as salts and alcohols) which cause a shift in the P_e-T_e equilibrium because of competition with the hydrate for guest and host molecules. Dissociation results in the production of gas and water, with a corresponding reduction in the saturation of the solid hydrate phase. For the case of methane hydrates, the endothermic dissociation reaction is:

$$CH_4 \cdot N_H H_2O \ (h) = CH_4 \ (g) + N_H H_2O \ (w), \tag{2}$$

where the hydration number N_H is approximately 6. Depending on the thermodynamic state, the water produced in the reaction of equation (2) can exist as liquid (the common product of dissociation in geologic systems) or ice.

Two approaches are possible for predicting hydrate dissociation. The first considers the reaction of equation (2) to occur at chemical equilibrium, while the second treats it as a kinetic reaction. The equilibrium relationship between P_e and T_e is described by Figure 1, which also includes the polynomial expression used for the computation of the P_e-T_e curve [4]. In the equilibrium model, the system is composed of heat and two mass components (CH_4 and H_2O) that are distributed among four possible phases: the gas phase (composed of CH_4 and H_2O vapor), the aqueous phase (composed of H_2O and dissolved CH_4), the solid

ice phase (involving exclusively H_2O), and the solid hydrate phase. Thus, the system always exists at equilibrium, with the occurrence of the various phases and phase transitions determined by the availability and relative distribution of heat and of the two components.

In the kinetic model, the system is composed of heat and three mass components: CH_4, H_2O, and $CH_4 \cdot N_H\ H_2O$. As opposed to the equilibrium model, the hydrate is not treated as a thermodynamic state of CH_4 and H_2O but as a third distinct compound. In this case the solid hydrate phase is considered to be composed exclusively of the $CH_4 \cdot N_H\ H_2O$ component. Phase changes and transitions are determined by a kinetic rate of dissociation or formation, which acts as a source/sink term and is given by the equation of *Kim et al.* [12]:

$$\frac{dm_H}{dt} = K_0 \exp\left(\frac{-E}{RT}\right) F_A A\left(f_e - f\right), \tag{3}$$

where f and f_e are the values of fugacity [Pa] for the pressure at temperature T [C] in the gas phase and at equilibrium, respectively; E is the hydration activation energy [J mol^{-1}]; K_0 is the hydration reaction constant [kg m^{-2} Pa^{-1} s^{-1}]; A is the surface area [m^2] for the reaction; F_A is the area adjustment factor [dimensionless], which accounts for deviations from the assumption of grain sphericity used in calculating A [5]; and R is the universal gas constant [J mol^{-1} C^{-1}]. Values of K_0 and the E have been determined from laboratory data in pure hydrate systems [12, 13] and in hydrate-bearing media [14].

It is difficult to know *a priori* which reaction model, equilibrium or kinetic, is most appropriate for the description of problems of hydrate dissociation in porous media. While the kinetic model may more accurately model hydrate dissociation, the use of the

equilibrium model may be justified in some cases due to its computational efficiency (as it involves one less equation per grid block than the kinetic one) and because predictions made using both models are in many cases remarkably similar [5]. Prior to this study, we worked with the assumption that, in general, thermal stimulation is accurately described by an equilibrium model, while a kinetic model may be more appropriate for depressurization-induced dissociation.

1.2. Objectives

The objective of this study is to investigate by means of numerical simulation the conditions under which the use of each of the two models (equilibrium or kinetic) is appropriate, and to evaluate differences in predictions from the two models. Specifically, we aim (1) to investigate whether the rate of CH_4-hydrate dissociation in a variety of realistic situations is limited by kinetics; (2) to compare model predictions obtained by using the kinetic and equilibrium models of dissociation for a wide range of production scenarios and geological settings; and (3) to investigate the relative sensitivity of the two dissociation models to a number of parameters, including domain discretization, initial hydrate saturation and the area adjustment factor F_A (Equation 3).

1.3. Test Cases

We investigate four test cases (A-D). The first two cases involve production from a Class 3 hydrate accumulation [15], which is characterized by a hydrate-bearing layer (HBL) underlain and overlain by impermeable layers. In Case A dissociation is induced by thermal stimulation, in which the temperature of the HBL is increased above T_e at the prevailing pressure (Figure 1), while in Case B dissociation in induced by depressurization, in which

the pressure of the HBL in reduced below the P_e at the prevailing temperature (Figure 1). In Case C we examine production at a constant rate from a Class 1 hydrate accumulation. This type of accumulation is characterized by a HBL overlain by an impermeable layer and underlain by a two-phase zone of water and mobile gas, and was identified as a particularly promising target for gas production [15,16]. In Case D, we simulate the response of a hydrate-bearing core as it is extracted from depth (in-situ conditions) and transported to the surface.

1.4. Numerical Simulator

The numerical studies in this paper were conducted using TOUGH-Fx/HYDRATE [5], which models the nonisothermal hydration reaction, phase behavior and flow of fluids and heat under conditions typical of natural CH_4-hydrate deposits in complex formations. It includes both equilibrium and kinetic models of hydrate formation and dissociation and can handle any combination of the possible hydrate dissociation mechanisms (i.e., depressurization, thermal stimulation, and inhibitor-induced effects). TOUGH-Fx/HYDRATE accounts for heat and up to four mass components (i.e., water, CH_4, hydrate, and water-soluble inhibitors such as salts or alcohols) that are partitioned among four possible phases (gas, liquid, ice or hydrate phases, which may exist individually or in any of 12 possible combinations).

2. Case A: Thermal-Stimulation-Inducted Production in Hydrate Accumulation

The HBL of the Class 3 hydrate accumulation in this case has a thickness of 10 m and involves a cylindrical domain with maximum radius r_{max} = 1000 m. The domain was divided into 600 grid blocks in the radial direction, beginning at the well radius r_w = 7.5 cm, and employing a spacing that is Δr = 0.05 m near the well and increases logarithmically with r away from the well. The initial hydrate and aqueous phase saturations (S_h and S_a, respectively) are spatially uniform, with $S_h = S_a = 0.5$, and the gas phase saturation $S_g = 0$. The most relevant properties of the model are listed in Table 1.

Thermal dissociation is expected to be most useful for cases in which the HBL contains high initial S_h, which corresponds to drastically reduced permeability (rendering depressurization methods impractical). Thermal stimulation is accomplished by maintaining the well at a constant pressure (equal to the initial HBL pressure) and an elevated temperature of T_W = 45 ^{o}C (see Table 1). Heat flows from the well into the HBL mainly by conduction at a rate that declines over time as the temperature in the vicinity of the well increases.

2.1. Pressure, Temperature and Phase Saturations

Figure 2 shows the radial distributions of pressure, temperature, and phase saturations after 30 days of heating, as obtained from simulations performed using the kinetic and equilibrium reaction models.

By this time, the temperature front (Figure 2a) has propagated into the HBL and induced dissociation over a distance of 1.3 m, resulting in the evolution of gas (originating exclusively from the hydrate, Figure 2b) and an increase in pressure (Figure 2a). In the region behind the dissociation front (r < 1.3 m), the hydrate has completely dissociated (S_h

= 0), while S_w and S_g have both increased (as water and gas are products of dissociation) from their initial values (Figure 2b). We observe a sharp increase in S_h over a short distance immediately ahead of the dissociation front (r > 1.3 m), mirrored by a corresponding sharp decline in S_a. This is caused by secondary hydrate formation ahead of the advancing front, caused by (a) outward flow of a fraction of the released gas (toward the HBL outer boundaries) and (b) the increased pressure (Figure 2a) at the dissociation front caused by the gas release. Beyond these saturation spikes, the phase saturations remain nearly equal to the initial conditions. Note that the pressure rise at the dissociation front indicates fluid flow in both directions and that the temperature distribution (Figure 2a) is marked by a slight discontinuity in the vicinity of the front.

The most important observation from reviewing Figure 2 is that, although slight deviations in the phase saturations and pressure are observed near the dissociation front (where the saturation spikes are observed), the profiles obtained from the kinetic and equilibrium reaction models are nearly identical.

2.2. Gas Release and Production Patterns

Figure 3 shows the gas release and production patterns for the kinetic and equilibrium dissociation models during the 30-day heating period. Specifically, the following quantities are examined: (a) the volumetric rate Q_R of CH_4 release into the formation (Figure 3a); (b) the volumetric rate Q_P of CH_4 production at the well (Figure 3b); and (c) the cumulative volumes V_R and V_P of CH_4 released in the formation and produced at the well, respectively (Figure 3c).

The rate of CH_4 released to the system during thermal stimulation is shown in Figure 3a. To facilitate comparison between the kinetic and equilibrium release rates, Q_R for the kinetic case is averaged in time using a moving window of 5 days. For both cases, Q_R is similar, approximately 50 m^3/day.

The periodic nature of Q_R in the equilibrium case (Figure 3a) is related to the spatial discretization of the domain. As the temperature front propagates through the system, individual grid blocks begin to warm sequentially. Dissociation in a given grid block begins when T increases above the hydration temperature T_e at the prevailing pressure P. Q_R initially increases with time as the grid block warms, and continues increasing until hydrate dissociation has reduced S_h to a point at which an increasing fraction of the incoming heat is expended in increasing the temperature of the porous medium rather than fueling dissociation. Q_R begins to decrease past that point. Dissociation does not progress significantly into the next grid block because of the steepness of the dissociation front (see Figure 2). Thus, the hydrate dissociation pattern exhibits the periodic pattern observed in Figures 3a and 3b, coinciding with the time for dissociation of individual grid blocks in the 1D radial system.

Note that Q_R becomes negative at some times (Figure 3a). This phenomenon results from the fact that the pressure increase caused by dissociation in a grid block causes gas to migrate into the adjacent grid block beyond the dissociation front, where the temperature is still relatively low, causing hydrate formation due to the increased pressure. This explains why S_h is increased to nearly 0.8 near the dissociation front in Figure 2b. The rate at which CH_4 is produced at the well (Q_P) is expected to be lower than Q_R since what is released to

the formation does not reach the production well instantaneously. Figure 3b shows that for both the kinetic and equilibrium cases, the production rates are very similar.

Similarly, the total volumes released from the formation and produced at the well (V_R and V_P, respectively) for both cases are found to be nearly identical for the kinetic and equilibrium cases (Figure 3c). Similar to the discussion above, V_P comprises the volume of gas that reached the well by a given time, and is therefore less than what is released to the entire system at that time.

2.3. Sensitivity to Initial Hydrate Saturation, Spatial Discretization and Reaction Area

In addition to the reference case with $S_h = 0.5$, we considered two additional values in order to determine the effect of hydrate saturation on the system response using the equilibrium and kinetic models. The V_R and V_P predictions using the equilibrium and the kinetic models follow the same pattern as those discussed above for the reference case (Figure 4). The predictions made when employing the equilibrium model are practically identical to those from the kinetic model for $S_h = 0.75$, while the two predictions exhibit only very minor differences for an initial $S_h = 0.25$.

In order to examine the sensitivity of the results to spatial discretization, we performed a simulation with coarser near-well discretization (0.10 m). In this case the Q_R and Q_P rates and the V_R and V_P volumes are similar for both dissociation models (Figure 3d-f). Compared to the simulation performed using finer discretization, the periodicity of Q_R approximately doubled (mirroring the increase in Δr) because of the longer time needed for the dissociation front to propagate through the length of each grid block. However, the total

volumes released to the system and produced at the well were similar to the finer discretization case.

Since the area available for heat transfer in the hydration reaction could conceivably cause differences between predictions made using the kinetic and equilibrium reaction models, we conducted a series of simulations with decreasing values of the area adjustment factor F_A (varying from the reference value of 1 to 0.001) to investigate the issue. The results in Figure 5a indicate that a kinetic model with decreasing F_A results in correspondingly lower production rates Q_P than those predicted in the equilibrium case. However, the Q_P predictions differ substantially only at very early times, and appear to converge for times greater than 1 day. Thus, with the exception of at early times or for very short study periods (e.g., which might apply to laboratory studies), Q_P appears to be independent of F_A (Figure 5a) in any practical scenario of thermally-induced dissociation. Note that the early Q_P differences observed for different F_A values appear inconsequential in the prediction of the overall production volume V_P in Figure 5b, which shows almost complete insensitivity to F_A. This is because the early Q_P differences persist for a very short time and involve very small volumes.

Predictions of thermally-induced gas dissociation and production are practically indistinguishable when using either the kinetic or the equilibrium model (including for varied levels of discretization, initial hydrate saturation, and reaction area in the kinetic model), implying that there is no kinetic limitation to gas production from HBL by means of thermal stimulation.

3. Case B: Depressurization-Induced Production in Hydrate Accumulation

The main difference between Cases A and B is the production method. In Case B production is induced by depressurization, an approach which is suitable in Class 3 hydrate accumulations if reasonably high fluid flow rates through the HBL are possible (i.e., for reasonably high intrinsic permeability and low initial hydrate saturation S_h). By withdrawing reservoir fluids at the well, the pressure in the HBL is made to decrease. Depressurization begins when the pressure in the HBL falls below the hydration pressure at the prevailing temperature in the HBL. Because the dissociation reaction is highly endothermic, the system can cool rapidly during depressurization, potentially creating ice, which can dramatically reduce the permeability of the system. To mitigate this effect by maintaining a warmer temperature, a constant source of heat is added at the well (this is accomplished in the model by setting a constant temperature at the well).

The HBL has a thickness of 10 m and is modeled in this case using radial coordinates with a maximum radius of 10,000 m and a total of 254 grid blocks. Radial spacing Δr begins at 5 cm and increases logarithmically away from the well. The initial phase saturations are similar to the previous case ($S_h = S_a = 0.5$, and $S_g = 0$). The most relevant properties of the model are listed in Table 1.

Below we discuss the overall behavior of a HBL undergoing depressurization-induced dissociation and evaluate the sensitivity of the predictions to the initial hydrate saturation and the area adjustment factor F_A.

3.1. Pressure, Temperature and Phase Saturations

The distributions of pressure and temperature are shown in Figure 6a for a simulation time of 30 days after the onset of depressurization. Whereas a sharp dissociation front (spanning a fraction of a meter) was evident in the case of thermal stimulation (Case A, Figure 2), depressurization results in a wide zone of dissociation (spanning tens of meters). This occurs because the propagation speed of the pressure front in a depressurization regime significantly exceeds that of the temperature front in thermal stimulation, thus inducing dissociation over large regions (spanning multiple grid blocks). As expected, the temperature decreases in the zone of dissociation (Figure 6a) due to the endothermic nature of the hydrate dissociation reaction.

The corresponding phase saturation profiles indicate that the hydrate has been completely dissociated for radii less than 3 meters, while the region between 3 and 80 meters is still undergoing dissociation (Figure 6b). Note that the distributions are nearly identical for both the equilibrium and kinetic models. Ice formation did not occur during this simulation.

3.2. Gas Release and Production Patterns

The CH_4 release and production rates Q_R and Q_P and cumulative volumes V_R and V_P for this case are shown in Figures 7a-c. Averaging of Q_R for the kinetic case was again performed using a moving window of 5 days in order to facilitate comparison of the kinetic and equilibrium cases (Figure 7a).

The production rate Q_P declines smoothly with time (Figure 7b), as opposed to the periodic response observed in the case of thermal stimulation (Case A, Figure 3b). This is caused by the wide dissociation zone created during depressurization which allows dissociation to occur simultaneously over a large region (and a large number of grid blocks).

The rates Q_P and Q_R are similar for both the kinetic and equilibrium reactions models (Figure 7c), as are the volumes V_R and V_P (Figure 7c). A slight difference in the volumes V_R is seen, though the relative difference decreases with time. In addition, the volumes produced at the well are nearly identical for both cases.

3.3. Sensitivity to Initial Hydrate Saturation and Reaction Area

Analogous to Figures 7a-c, the sensitivity of the differences between reaction models for lower initial hydrate saturation is shown in Figures 7d-f. The overall affect of decreasing the initial S_h is a decline in V_P, which results from the decreased amount of hydrate available for dissociation (compare Figures 7b and 7e). Note that lower S_h leads to larger Q_R discrepancies, though still relatively small, between kinetic and equilibrium predictions.

The early-time (less than 1 day) production rates are given in Figure 8 for two cases of initial hydrate saturation and for values of the area adjustment factor F_A decreasing by up to three orders of magnitude. For the case of initially lower S_h (Figure 8b), the production rate increases at first more rapidly and to a higher value than for the case of initially higher S_h (Figure 8a). The relative permeability of the system is higher in the lower saturation case allowing gas to reach the production well more quickly. By simulation time t = 1 day, however, this trend reverses, with the production rate for the lower saturation case decreasing faster and remaining lower than for the higher saturation case due to the decreased amount of hydrate available for dissociation.

Decreasing F_A in the kinetic reaction model delays and decreases the early-time rise in production relative to the equilibrium case, though the decrease is relatively larger with

lower hydrate saturation. The effect of F_A is seen to only be a factor for early times ($t < 0.1$ days).

Similar to the case of thermal stimulation, there appears to be no kinetic limitation to gas production from Class 3 hydrates by means of depressurization-induced hydrate dissociation over time frames relevant to production. However, accounting for kinetic effects may be important for modeling very short-term processes, such as laboratory experiments.

4. Case C: Constant-Rate Production in Hydrate Accumulation

This case involves production in a Class 1 hydrate system in which a 15 meter thick HBL underlies an impermeable layer and overlies a 15 meter thick two-phase zone of gas and water (Figure 9). The upper and lower impermeable (clay) layers permit the flow of heat but not fluids.

The hydrate system is modeled using a 2D cylindrical domain with a maximum radius of 550 m and a vertical span of 90 m. Discretization in the vertical direction equals 25 cm in the HBL and 1 m in the two-phase zone, and ranges between 25 cm and 7 m in the impermeable layers. Radial spacing Δr increases gradually from 15 cm to 35 m.

Initially, the hydrate saturation in the HBL equals 0.7. The distributions of aqueous and gas saturation in the HBL and in the underlying zone are non-uniform and determined using the equilibration procedure discussed in [16]. Fluids are withdrawn at a constant mass rate over a screened portion of the well (see Figure 9). To alleviate the possibility of secondary

hydrate formation in the vicinity of the well during production, heat is added to the well over the screened region.

In order to obtain an equilibrated model that maintains the temperature and position (typically known) at the bottom of the HBL, the appropriate boundary conditions and initial conditions must be determined. For this purpose we use a two-step equilibration procedure [16]. See Table 2 for a description of the most relevant model parameters used in this simulation.

Figures 10a-c show the phase saturation distributions at after 2 months. The respective differences between the kinetic and equilibrium models are shown in Figures 10d-f. The main differences occur in the vicinity of the dissociation front over a narrow band.

4.1. System Response during Production

The predicted Q_R curves from the equilibrium and kinetic reaction models over the 2-month simulation period are shown in Figure 11a. During the first day, the Q_R rates for both models are in close agreement; the rate for the kinetic model slightly fluctuates around the smoothly varying rate of the equilibrium model. At later times, Q_R for the kinetic case rises gradually with small-scale fluctuations. In contrast, much larger fluctuations are observed for the equilibrium case, beginning at the t = 1 day and continuing for about 45 days, because the equilibrium model is less thermodynamically stable than the kinetic model. Small changes in thermophysical properties and conditions (Pressure, temperature and saturations) can result in abrupt changes, introducing slight overshooting of primary variables. Though this is corrected in the next time step, in which the imbalance caused by the drastic swing is redressed by a state and phase reversal. Figure 11 exhibits the

significant fluctuations, which are pronounced during the early stages of production (when the most abrupt changes occur). However, note that these fluctuations revolve about a mean, which very closely follows the kinetic prediction. After 45 days, the kinetic and equilibrium models once again tend toward the same rate.

The released volumes V_R for the kinetic and the equilibrium models (corresponding to the Q_R in Figure 11a) are shown in Figure 11b. The volumes of released gas continuously increase for both cases, though that for the kinetic case initially lags slightly behind (the relative difference is 15% at 60 days, and is the maximum deviation to be observed during the simulation); the relative difference between released gas volumes is expected to decrease with simulation times greater than 60 days, considering that release rates have reached a similar level by 60 days (Figure 11a). This is supported by the derivative dV_R/dt values, which are nearly the same for the kinetic and equilibrium models by 60 days.

For this case we conclude that (a) measurable (but still small) deviations between kinetic and equilibrium predictions are observed only at very early times (at which the deviations are at their maximum level), and (b) there appears to be no kinetic limitation to gas production from hydrates by means of depressurization in realistic production scenarios from Class 1 accumulations.

5. Case D: Response of Hydrate-Bearing Core during Extraction

In this case we examine the response of a hydrate core as it is raised from a HBL at a depth of 700 m to the surface. Understanding the behavior of hydrate-bearing samples during and

after core recovery is of great importance since detection of cores is used in practice to infer the presence and amount of hydrate in the subsurface.

The core modeled in this study has a length L = 3.0 m and a radius of 3.13 cm. Neglecting the effects of gravity across the length of the core, we take advantage of symmetry and model only half of it (Figure 12). Using a very fine grid to describe the domain, discretization along the vertical axis ranges between $\Delta z = 0.5$ cm and $\Delta z = 1$ cm, while discretization in the radial direction is even finer, ranging between $\Delta r = 0.1$ cm and $\Delta r = 0.2$ cm. A description of the model properties used in this simulation is given in Table 2.

The core is assumed to have uniform initial conditions of P = 9.372 MPa and T = 12 ^{o}C, and uniform phase saturations of $S_h = S_a = 0.5$ and $S_g = 0$. The bottom of the core (and the top, given the symmetry) is in contact with drilling mud, which is assumed to remain at a constant temperature of 2 ^{o}C. (In addition, a thin gap between the core and the mud is modeled at the outer radius of the core, allowing additional contact between the drilling mud and the core.)

To simulate the decreasing pressure to which the core is exposed (and which is the main dissociation-inducing mechanism) as it is raised in the borehole toward the surface, a time-varying boundary condition was applied to the portion of the core in direct contact with the mud. The time-variable boundary involved a linearly decreasing pressure from its initial level of $P_0 = 9.372$ MPa to the atmospheric pressure (P = 0.101 MPa) over a period of 20 minutes (a reasonable time for the core to reach the surface).

5.1. Evolution of Phase Saturations

The evolution of the phase saturations with time, as predicted by the equilibrium model, is shown in Figure 13. No hydrate dissociation is observed in the first 12.5 minutes of the core ascending the wellbore. At time t = 15 min, the effects of dissociation are evident (Figure 13a), and are most pronounced at the parts of the core in direct contact with the variable-pressure boundary, i.e., the core ends (top or bottom, given the symmetry of the problem) and the outer perimeter of the core (where the core barrel provides an imperfect seal at approximately r = 3 cm in Figure 13). Hydrate dissociation then proceeds rapidly, advancing by 0.4 m in 2.5 min (from t = 15.0 min to t = 17.5 min), and another 0.35 m in the next 2.5 min (from t = 17.5 min to t = 20 min).

This case differs from the previous ones in that the formation of ice occurs. Ice forms because of the rapid temperature drop caused by the strongly endothermic reaction of hydrate dissociation (Figure 13b). The water saturation (Figure 13c) decreases in the regions where both ice formation and gas evolution occur because it is expelled as ice expands. The expelled water accumulates near the perimeter of the core barrel and at the ends of the core (only one end is depicted in Figure 13, at the bottom of each plot), where a higher S_a is observed. Note the heterogeneous distribution of the S_i and S_a once ice begins forming.

The corresponding phase saturation distributions for the kinetic reaction model are shown in Figure 13d-f. Note that the onset of hydrate dissociation is delayed (Figure 13d) relative to the equilibrium case. Moreover, dissociation now occurs over a large zone, creating a smooth transition from the hydrate-free region at the bottom of the core to the region where hydrate remains (as opposed to the sharp boundary observed in Figure 13a). The ice

distribution is similarly smoothly varying (Figure 13e), as are the distributions of water saturation (Figures 13f).

Similar to Case C, thermodynamic instability and abrupt changes occur in response to the imposition of the equilibrium model. Because of the small grid blocks and the sensitivity to pressure and temperature, dissociation leads to ice formation and phase distribution adjustments (often abrupt) that satisfy equilibrium. This cannot be corrected within the same grid block in the next time step (because of the slow response of the solid phases, especially ice), but it is expressed in an adjacent grid block, thus keeping the entire system in balance. Thus, the rapid dissociation and emergence of ice significantly change the phase distribution patterns.

5.2. System Response during Production

The rate of methane release from the core during its 20 minute ascent to the surface is shown in Figure 14a. The corresponding volume fraction of CH_4 released from the core during this process is shown in Figure 14b. Note that the use of the equilibrium reaction model for this case would result in significant overestimation of the amount of hydrate lost during core extraction, assuming that the kinetic model is accurate.

In a short-term process such as the rapid core recovery, kinetic limitations can be important and ignoring them may lead to serious under-predictions of the recoverable hydrate in cores.

6. Summary and Conclusions

The objectives of this paper were to evaluate through numerical simulation the importance of employing kinetic versus equilibrium reaction models for predicting the behavior of hydrate-bearing systems in a variety of settings. Four test cases were considered.

The first case (Case A) involved thermal stimulation in a Class 3 hydrate accumulation. Predictions of thermally-induced gas dissociation and production were practically indistinguishable when using either the kinetic or the equilibrium model (including for varied levels of discretization, initial hydrate saturation, and reaction area in the kinetic model), and there appears to be no kinetic limitation to gas production from HBL by means of thermal stimulation. As seen in the second case (Case B), which also considered a Class 3 hydrate accumulation, there also appears to be no kinetic limitation to gas hydrate production from depressurization-induced production.

The third case (Case C) considered constant rate production in a Class 1 hydrate accumulation. Small deviations between kinetic and equilibrium predictions were observed only at very early times. For time scales of interest in production, there appears to be no kinetic limitation to gas production from hydrates in realistic production scenarios from Class 1 hydrate accumulations.

The fourth case (Case D) examined the response of a hydrate-bearing core during rapid core-recovery. This case represents one scenario in which the choice of reaction model is of great consequence. In a short-term process, such as this one, kinetic limitations can be important, and ignoring them may lead to significant under-prediction of the recoverable hydrate in cores.

It should be noted that the kinetic processes describing hydrate dissociation are incompletely understood, and that further advances may impact the results described here, though not necessarily the conclusions. For example, it may be possible to improve the model developed by Kim and Bishnoi [12], as given in Equation 3, as it is based on a relatively simple first-order rate law, and the dissociation experiments performed in order to develop it were conducted under conditions considerably far from equilibrium, which may serve as a potential source of bias. Furthermore, the model does not account for potential nucleation phenomena, resulting in instantaneous formation of gas hydrates, which may affect the simulated processes we observe occurring at the dissociation front during production.

In conclusion, assuming validity of the most accurate kinetic model that is currently available for modeling the dissociation of gas hydrates in porous media, the results of this study indicate: (1) the equilibrium reaction model is a viable alternative to the kinetic model for a wide range of large-scale production simulations; and (2) the kinetic reaction model appears to be important for accurately modeling short-term and core-scale simulations.

Acknowledgements

This work was supported by the Assistant Secretary of Fossil Energy, Office of Natural Gas and Petroleum Technology, through the National Energy Technology Laboratory, under the U.S. Department of Energy, Contract No. DE-AC03-76SF00098. The authors would also like to thank Yongkoo Seol and two anonymous reviewers for their helpful comments and suggestions.

Figure Captions

Figure 1. The phase diagram of the water-CH_4-hydrate system [4]. The existence of aqueous (Lw), ice (I), gas (V), and hydrate (H) phases, and combinations thereof, are indicated.

Figure 2. Simulated distributions at 30 days in Class 3 hydrate accumulation undergoing thermal stimulation: (a) pressure P and temperature T; and (b) hydrate saturation S_h, aqueous saturation S_a, and gas saturation S_g. Ice formation does not occur during this simulation ($S_i = 0$).

Figure 3. System response to thermal stimulation. The volumetric rate of CH_4 (a) released from the formation, (b) produced at the well, and (c) the corresponding total volumes of CH_4 released from the accumulation and produced at the well for near-well discretization of 5 cm. Corresponding plots are shown in (d) – (f) for the case of increased near-well discretization to 10 cm.

Figure 4. Effect of initial hydrate saturation S_h on the volume of CH_4 released from hydrate formation and produced at the well during thermal stimulation in Class 3 hydrate accumulation. The lower two curves correspond to $S_h = 0.25$, while the upper two correspond to $S_h = 0.75$.

Figure 5. Effect of reaction area on early-time response of Class 3 hydrate accumulation undergoing thermal stimulation. Values of decreasing F_A are indicated. Initial hydrate saturation $S_h = 0.5$.

Figure 6. Simulated distributions at 30 days in Class 3 hydrate accumulation undergoing depressurization-induced dissociation: (a) pressure P and temperature T; and (b) hydrate

saturation S_h, aqueous saturation S_a, and gas saturation S_g. Ice formation does not occur during this simulation ($S_i = 0$).

Figure 7. System response to depressurization in Class 3 hydrate accumulation. The volumetric rate of CH_4 (a) released from the accumulation, (b) produced at the well, and (c) the corresponding total volumes of CH_4 released from the accumulation and produced at the well for initial hydrate saturation $S_h = 0.5$. To facilitate comparison in (a), the kinetic release rate is averaged in time using a moving window of 5 days. Corresponding plots for initial hydrate saturation $S_h = 0.25$ are shown in (d) – (f).

Figure 8. Effect of reaction area on early-time CH_4 production rate in Class 3 hydrate accumulation undergoing depressurization for the case of (a) $S_h = 0.5$, and (b) $S_h = 0.25$ using both kinetic and equilibrium reaction models. Values of decreasing area adjustment factor F_A are indicated.

Figure 9. Schematic for Class 1 hydrate accumulation in which constant-rate production is simulated.

Figure 10. Simulated distributions at 60 days in Class 1 hydrate accumulation undergoing constant-rate production. The hydrate saturation S_h, gas saturation S_g, and aqueous saturation S_a profiles simulated using the kinetic reaction model are shown in (a) – (c). The corresponding differences (ΔS_h , ΔS_g and ΔS_a) between profiles simulated using kinetic and equilibrium reaction models are shown in (d) – (f) (i.e., the saturation for the kinetic case subtracted by the saturation distributions for the equilibrium case is shown).

Figure 11. Constant rate production in Class 1 deposit: comparison of CH_4 (a) release rates and (b) total volumes released from the accumulation for equilibrium and kinetic reaction models.

Figure 12. Schematic for hydrate-bearing core simulation. The initial conditions and some relevant parameters for the hydrate core, the drilling mud, and the core barrel are indicated.

Figure 13. Evolution of the distribution of phases during transport to the surface from a depth of 700 meters simulated using the equilibrium reaction model: a) hydrate saturation S_h, b) ice saturation S_i, c) aqueous phase saturation S_a. The corresponding cases for the kinetic reaction model are shown in (d) – (f)

Figure 14. Response of core during transport to the surface from a depth of 700 meters: (a) the rate at which CH_4 is released from the core and (b) the total volume of CH_4 released.

Figures

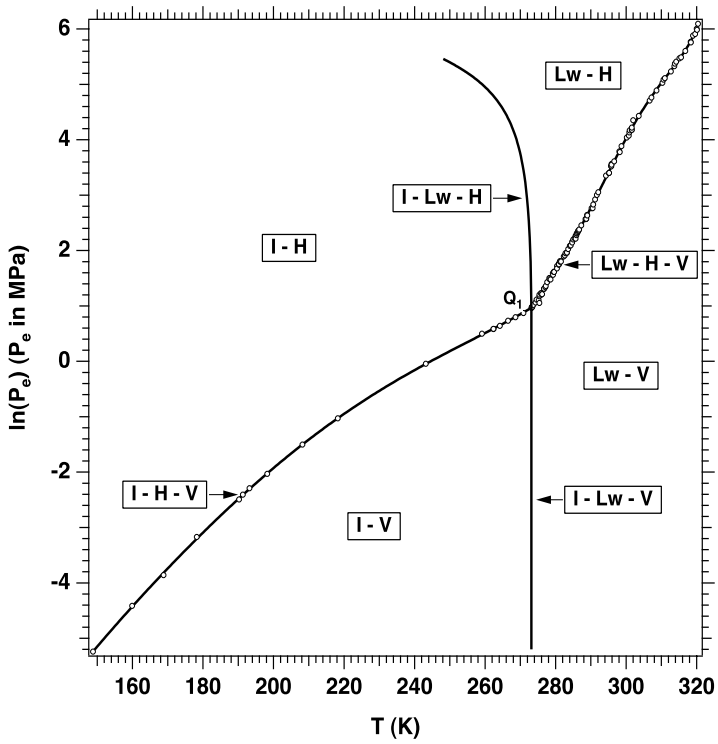

Figure 1.

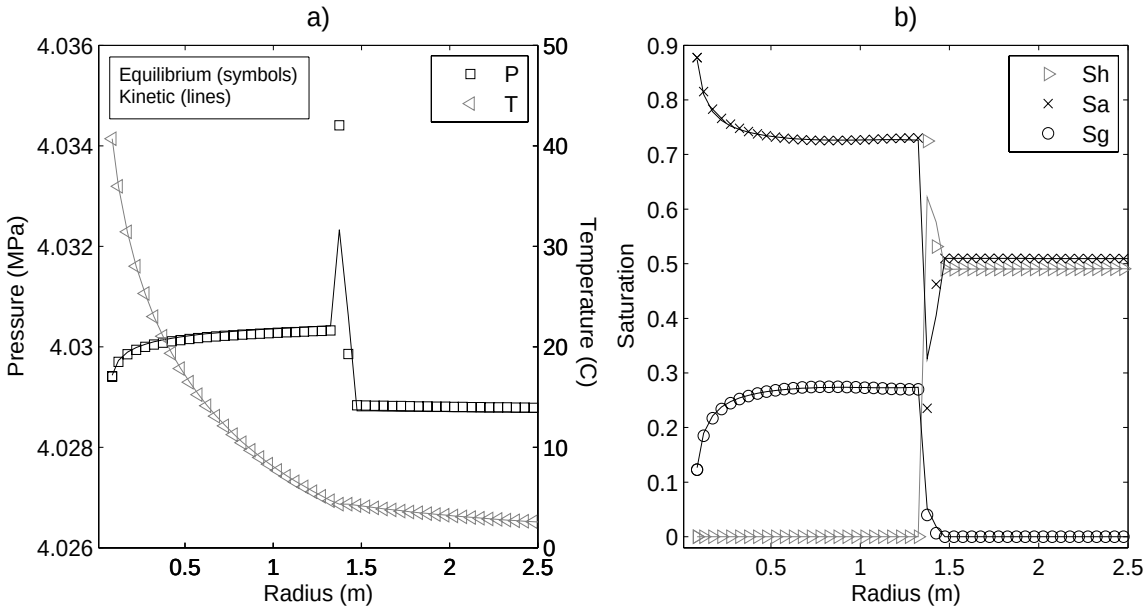
a)
b)
Equilibrium (symbols)
Kinetic (lines)
P
T
Pressure (MPa)
Temperature (C)
Radius (m)
Sh
Sa
Sg
Saturation
Radius (m)

Figure 2.

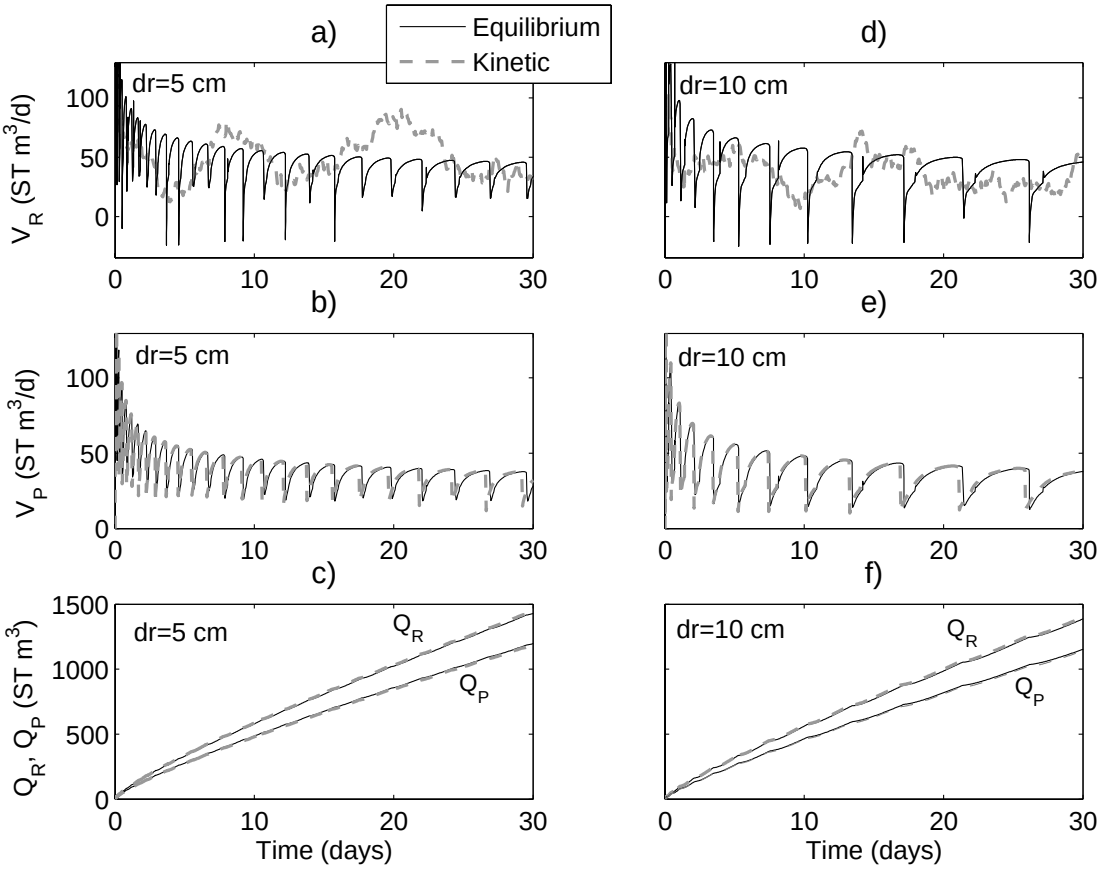
a)
Equilibrium
Kinetic
dr=5 cm
V_R (ST m^3/d)
d)
dr=10 cm
b)
dr=5 cm
V_P (ST m^3/d)
e)
dr=10 cm
c)
dr=5 cm
Q_R
Q_P
Q_R, Q_P (ST m^3)
Time (days)
f)
dr=10 cm
Q_R
Q_P
Time (days)

Figure 3.

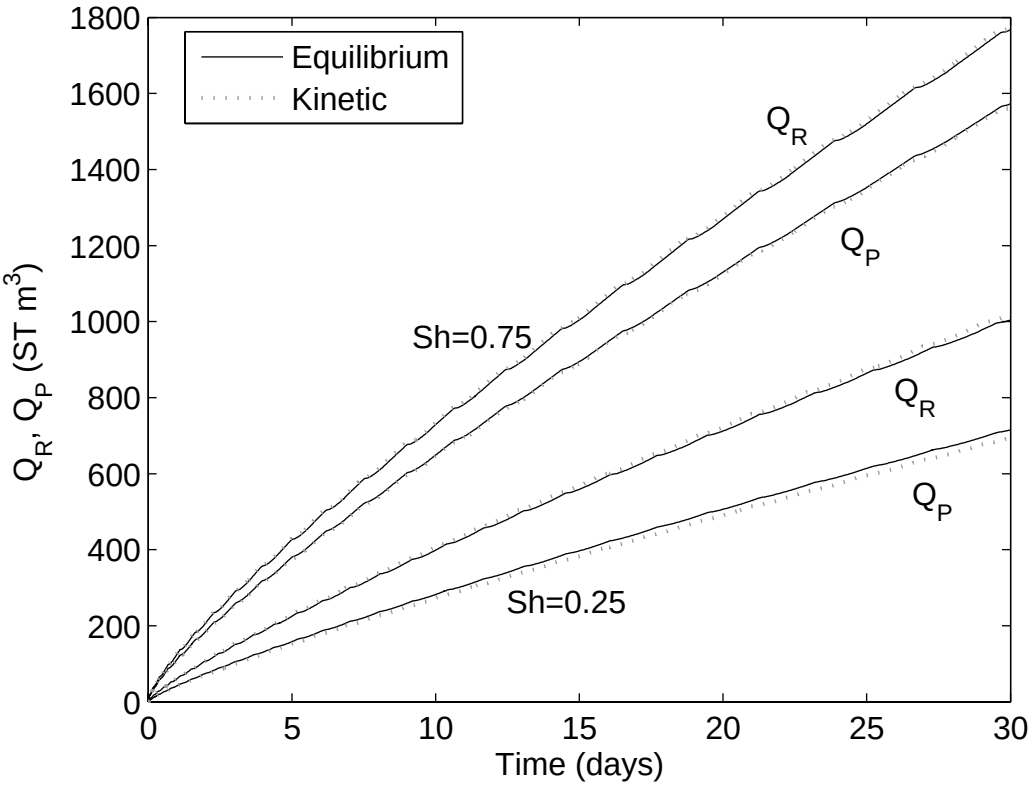
Equilibrium
Kinetic
Q_R
Q_P
Sh=0.75
Q_R
Q_P
Sh=0.25
Q_R, Q_P (ST m^3)
Time (days)
0
200
400
600
800
1000
1200
1400
1600
1800
0
5
10
15
20
25
30

Figure 4.

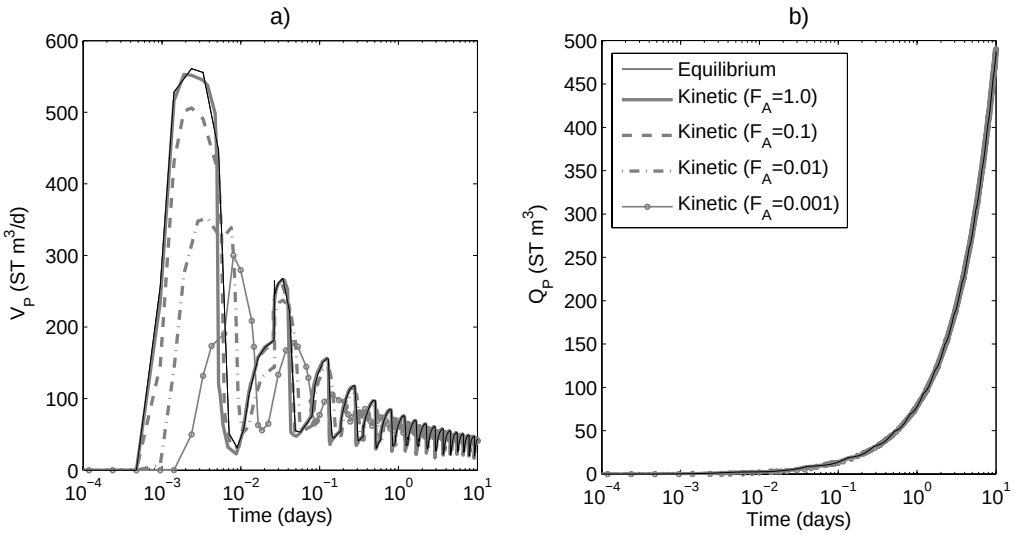
a)
b)
V_P (ST m^3/d)
Q_P (ST m^3)
Time (days)
Time (days)
Equilibrium
Kinetic (F_A=1.0)
Kinetic (F_A=0.1)
Kinetic (F_A=0.01)
Kinetic (F_A=0.001)

Figure 5.

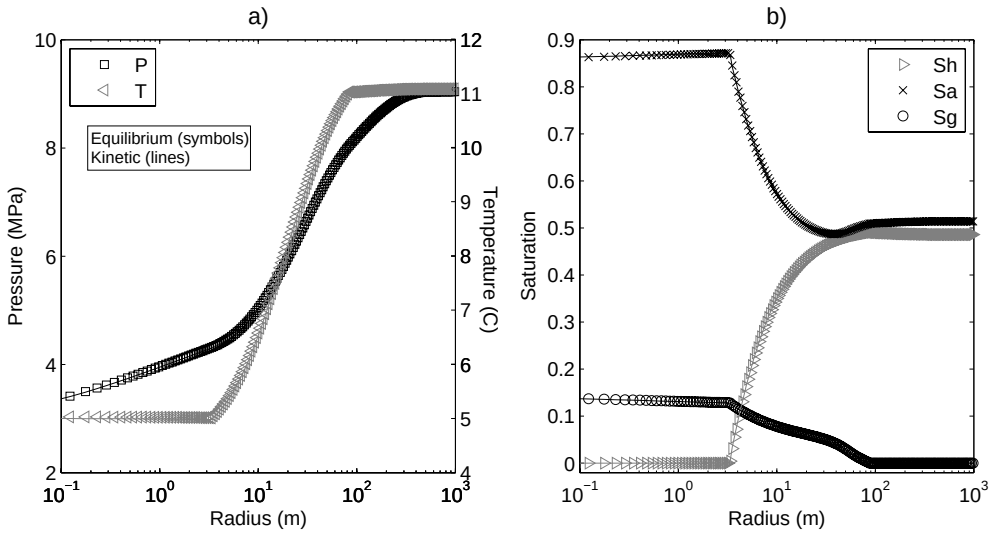
a)
b)
P
T
Equilibrium (symbols)
Kinetic (lines)
Pressure (MPa)
Temperature (C)
Radius (m)
Sh
Sa
Sg
Saturation
Radius (m)

Figure 6.

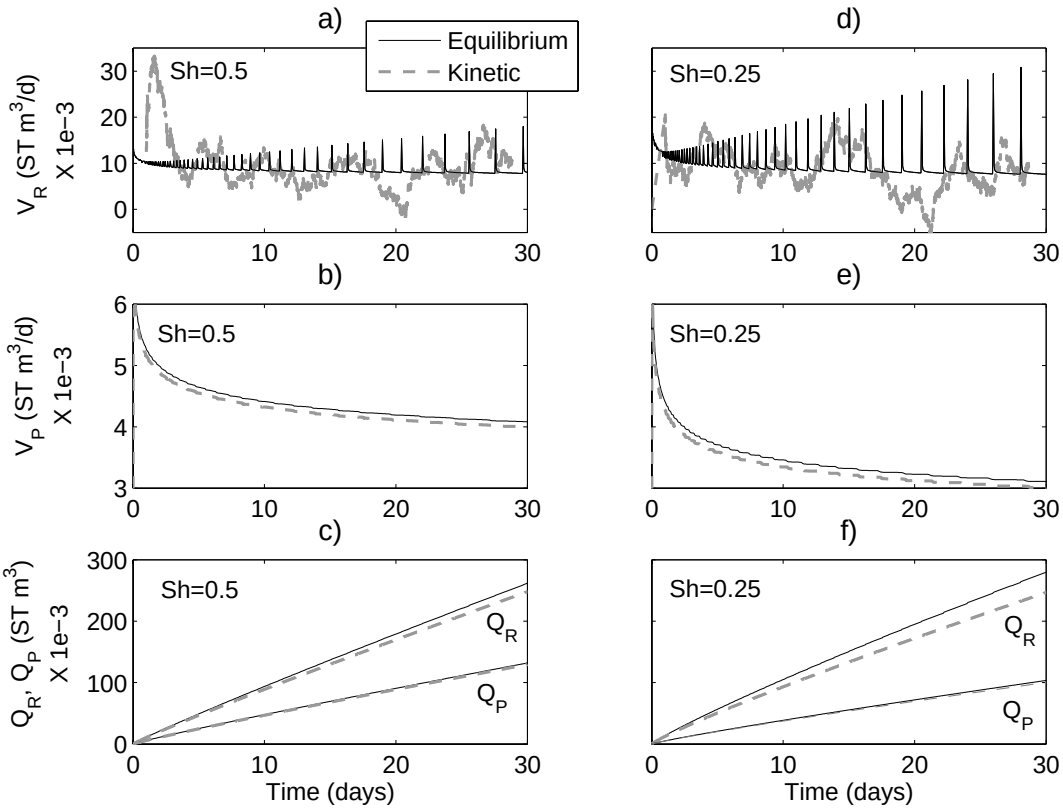
a)
Equilibrium
Kinetic
Sh=0.5
V_R (ST m^3/d)
X 1e−3
d)
Sh=0.25
b)
Sh=0.5
V_P (ST m^3/d)
X 1e−3
e)
Sh=0.25
c)
Sh=0.5
Q_R
Q_P
Q_R, Q_P (ST m^3)
X 1e−3
Time (days)
f)
Sh=0.25
Q_R
Q_P
Time (days)

Figure 7.

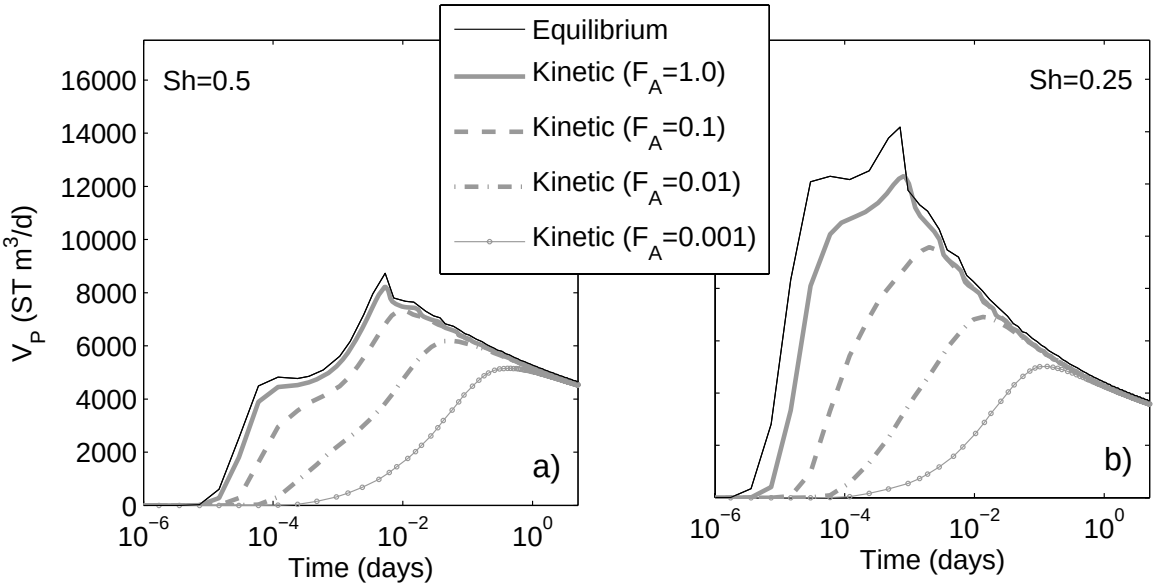
Equilibrium
Kinetic (F_A=1.0)
Kinetic (F_A=0.1)
Kinetic (F_A=0.01)
Kinetic (F_A=0.001)
Sh=0.5
Sh=0.25
V_P (ST m^3/d)
16000
14000
12000
10000
8000
6000
4000
2000
0
10^{-6}
10^{-4}
10^{-2}
10^{0}
Time (days)
a)
b)

Figure 8.

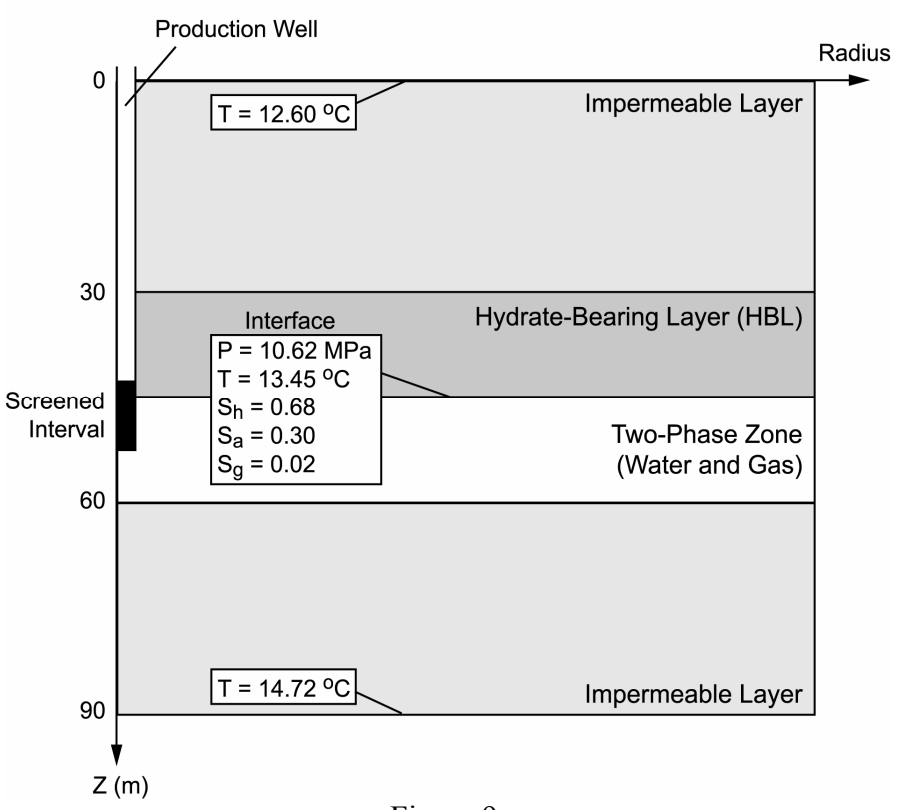
Production Well
Radius
0
T = 12.60 °C
Impermeable Layer
30
Interface
P = 10.62 MPa
T = 13.45 °C
S_h = 0.68
S_a = 0.30
S_g = 0.02
Hydrate-Bearing Layer (HBL)
Screened Interval
Two-Phase Zone (Water and Gas)
60
T = 14.72 °C
Impermeable Layer
90
Z (m)

Figure 9.

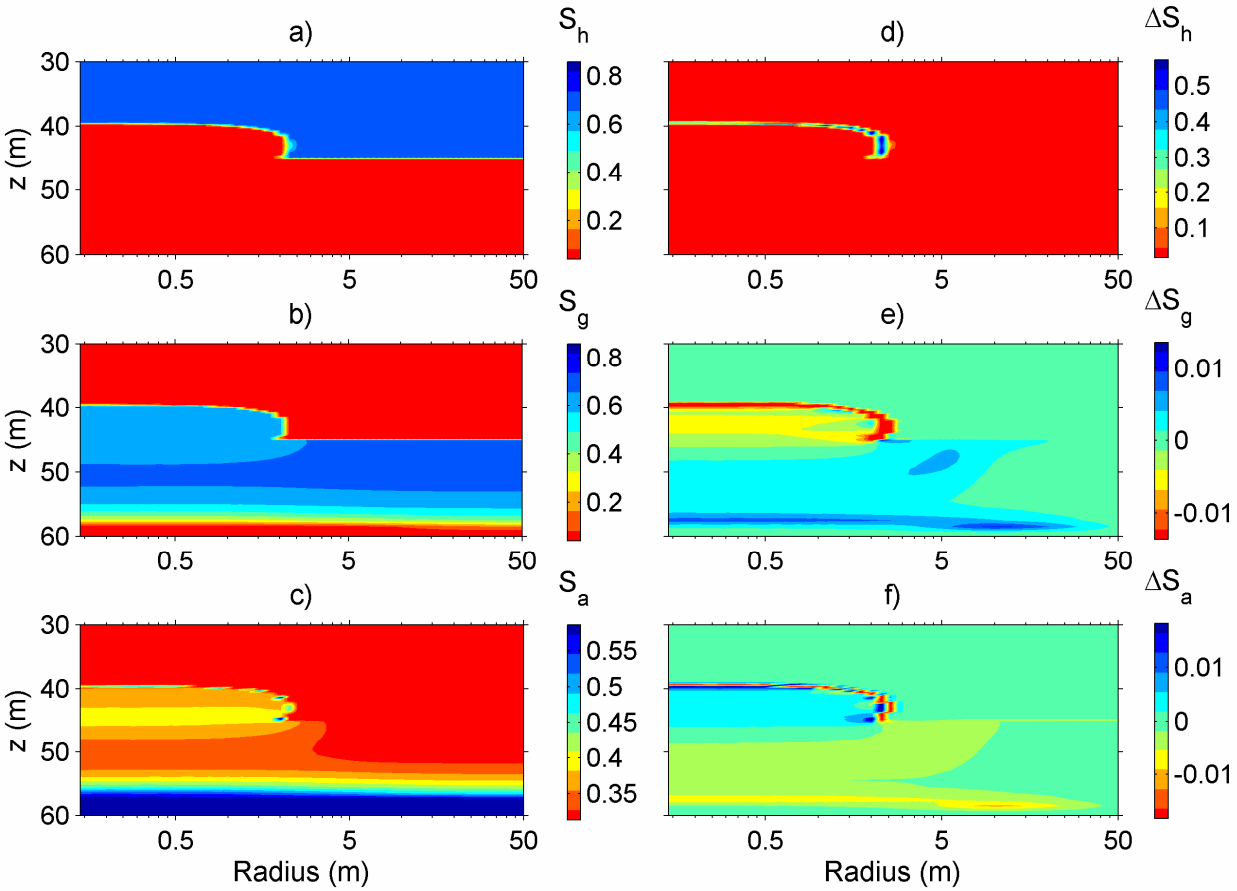
a)
b)
c)
d)
e)
f)
z (m)
Radius (m)
0.5
5
50
30
40
50
60
S_h
S_g
S_a
ΔS_h
ΔS_g
ΔS_a
0.8
0.6
0.4
0.2
0.55
0.5
0.45
0.35
0.1
0.3
0.01
0
-0.01

Figure 10.

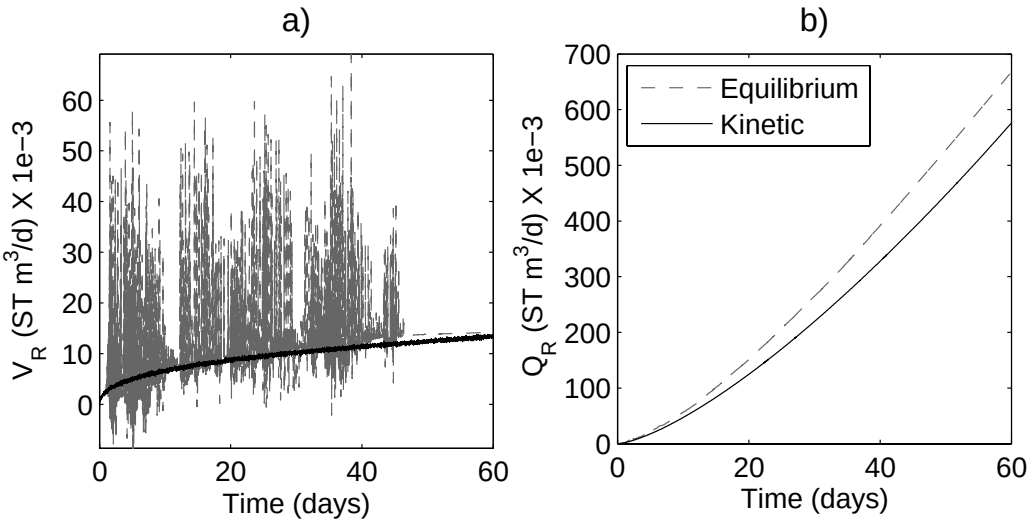
a)
b)
V_R (ST m^3/d) X 1e−3
Q_R (ST m^3/d) X 1e−3
Time (days)
Time (days)
Equilibrium
Kinetic
0
10
20
30
40
50
60
100
200
300
400
500
600
700
0
20
40
60

Figure 11.

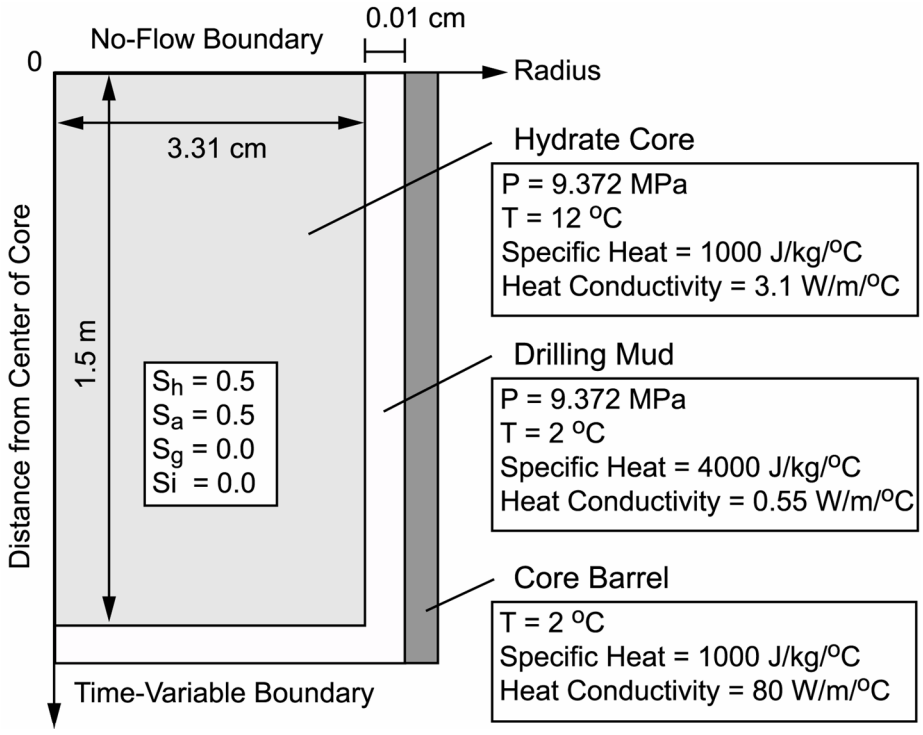
0.01 cm
No-Flow Boundary
0
Radius
3.31 cm
Hydrate Core
P = 9.372 MPa
T = 12 °C
Specific Heat = 1000 J/kg/°C
Heat Conductivity = 3.1 W/m/°C
Distance from Center of Core
1.5 m
Sh = 0.5
Sa = 0.5
Sg = 0.0
Si = 0.0
Drilling Mud
P = 9.372 MPa
T = 2 °C
Specific Heat = 4000 J/kg/°C
Heat Conductivity = 0.55 W/m/°C
Core Barrel
T = 2 °C
Specific Heat = 1000 J/kg/°C
Heat Conductivity = 80 W/m/°C
Time-Variable Boundary

Figure 12.

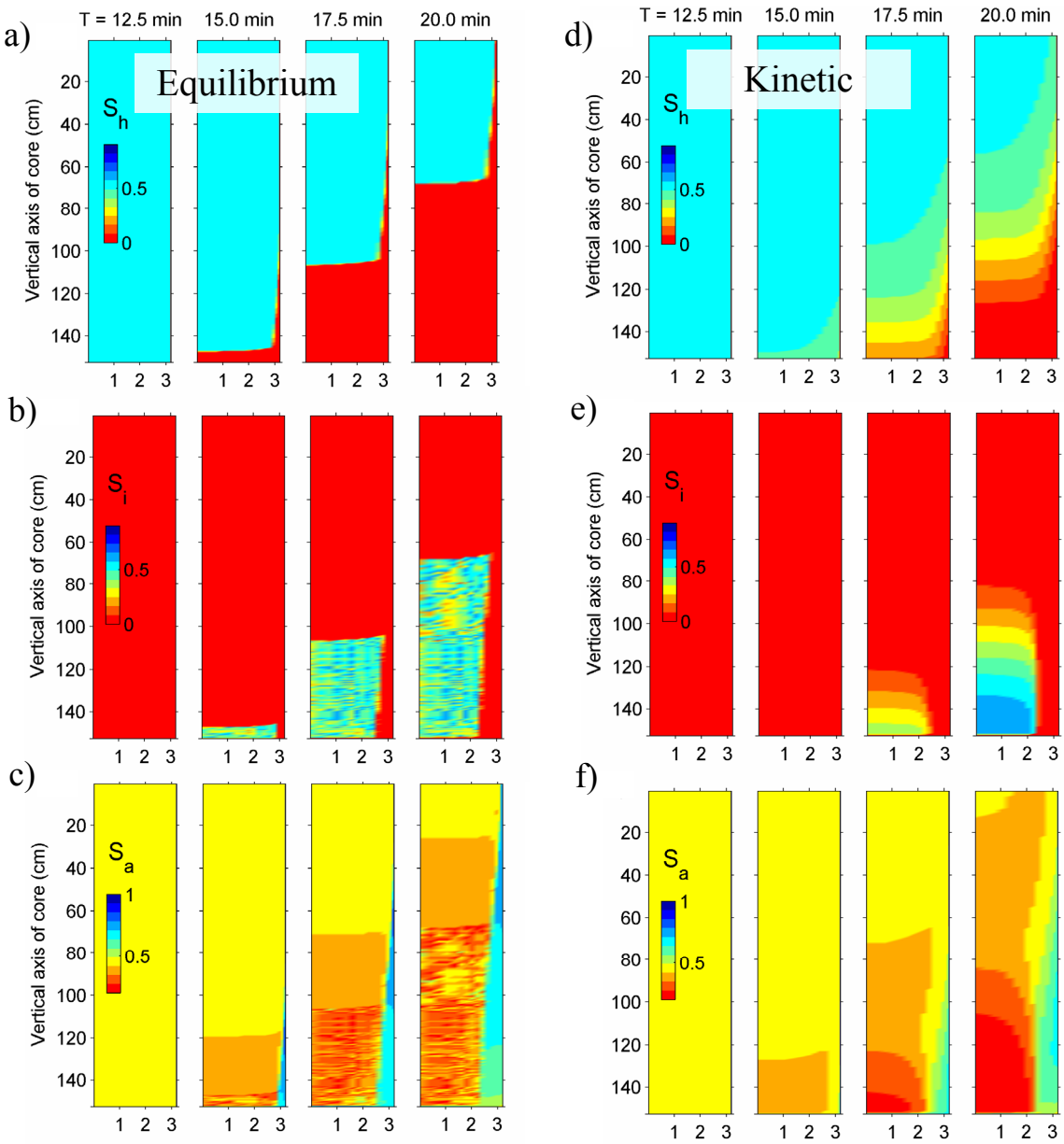
a)
T = 12.5 min
15.0 min
17.5 min
20.0 min
Equilibrium
S_h
0.5
0
Vertical axis of core (cm)
b)
S_i
c)
S_a
1
d)
Kinetic
e)
f)

Figure 13.

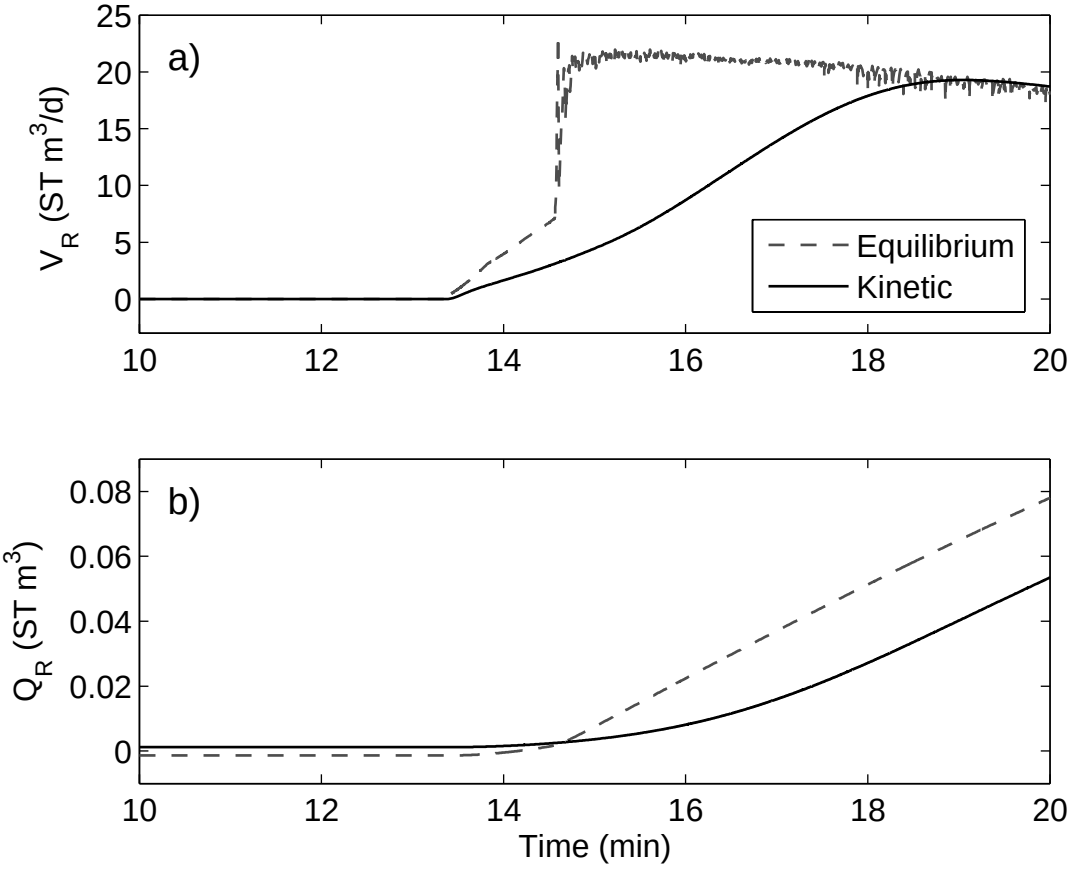
a)
b)
V_R (ST m^3/d)
Q_R (ST m^3)
Time (min)
Equilibrium
Kinetic
25
20
15
10
5
0
0.08
0.06
0.04
0.02
0
10
12
14
16
18
20

Figure 14.

Table 1. Parameters for simulation of Class 3 hydrate accumulations (Cases A and B).

Parameter	Case A	Case B
Description of problem	Thermal stimulation in Class 3 hydrate accumulation	Depressurization in Class 3 hydrate accumulation
HBL thickness	10 m	*N/C*[1]
Initial pressure P	4.028×10^6 Pa	9.039×10^6 Pa
Initial temperature T	1.06 °C	11.08 °C
Constant well pressure P_{well}	4.028×10^6 Pa	2.7×10^6 Pa
Constant well temperature T_{well}	45 °C	11.08 °C
Initial water saturation S_a	0.5	0.5
Initial hydrate saturation S_h	0.5	0.5
Initial gas saturation S_g	0.0	*N/C*
Porosity	0.30	*N/C*
Permeability	2.96×10^{-13} m^2	*N/C*
Grain density	2,600 kg/m^3	*N/C*
Wet thermal conductivity	3.1 W/m/°C	*N/C*
Dry thermal conductivity	0.5 W/m/ °C	*N/C*
Capillary pressure model[2] $P_{cap} = -P_o[(S^*)^{-1/\lambda} - 1]^{-\lambda}$ $S^* = (S_a - S_{a,r})/(S_{a,max} - S_{a,r})$	$S_{a,max} = 1.0$, $\lambda = 0.6$ $P_o = 1{,}887.0$ Pa	$S_{a,max} = 1.0$, $\lambda = 0.45$ $P_o = 1.25 \times 10^4$ Pa
Relative permeability model[3] $k_{r,a} = [(S_a - S_{a,r})/(1 - S_{a,r})]^n$ $k_{r,g} = [(S_g - S_{g,r})/(1 - S_{a,r})]^n$	$n = 3.0$ $S_{g,r} = 0.02$ $S_{a,r} = 0.12$	*N/C*
Kinetic reaction parameters		
Activation energy E	8.1×10^4 J/mol	*N/C*
Intrinsic rate constant K_0	3.6×10^4 kg m^{-2} Pa^{-1} s^{-1}	*N/C*
Area Factor F_A	1.0	*N/C*

[1] *N/C* indicates no change from previous value.
[2] See [17] and [5] for details.
[3] The effects of emerging fluid and solid phases on permeability are accounted for using the first Evolving Porous Medium (EPM) model of Moridis et al. [5]. The permeability calculated with this model is also used to scale pressure [18].

Table 2. Parameters for simulation of Class 1 hydrate accumulation and extraction of hydrate-bearing core (Cases C and D).

Parameter	Case C	Case D
Description of problem	Constant-rate production in Class 1 hydrate accumulation	Recovery of Hydrate Core from depth of 700 meters
Initial pressure P	*(See Section 4)*	9.372×10^{6} Pa
Initial temperature T	*(See Section 4)*	12 °C
Production Rate	5.55×10^{-2} kg/s	*N/A*[1]
Heat Injection Rate	12.5 J/s	*N/A*
Initial water saturation S_a	*(See Section 4)*	*(See Section 5)*
Initial hydrate saturation S_h	*(See Section 4)*	*(See Section 5)*
Initial gas saturation S_g	*(See Section 4)*	*(See Section 5)*
Porosity	0.30	0.30
Permeability	1.0×10^{-12} m^2	2.96×10^{-13} m^2
Grain density	2,600 kg/m^3	*N/C*[1]
Wet thermal conductivity	3.1 W/m/°C	*N/C*
Dry thermal conductivity	0.5 W/m/ °C	*N/C*
Capillary pressure model[2] $P_{cap} = -P_o[(S^*)^{-1/\lambda} - 1]^{-\lambda}$ $S^* = (S_a - S_{a,r})/(S_{a,max} - S_{a,r})$	*N/A*	$S_{a,max} = 1.0$ $\lambda = 0.45$ $P_o = 2{,}000$ Pa
Capillary pressure model[3] $P_{cap} = -F \cdot G \cdot P_{GE}(S^*)^{\nu}$ $F = 1 + A \cdot Bx(a, b, S_H)$ $S^* = (S_a - S_{a,r})/(1 - S_{a,r})$	$\nu = -0.7$ $A = 9.28$ $a = 2.1$ $b = 2.2$	*N/A*
Relative permeability model[4] $k_{r,a} = [(S_a - S_{a,r})/(1 - S_{a,r})]^n$ $k_{r,g} = [(S_g - S_{g,r})/(1 - S_{a,r})]^n$	*n = 3.0* $S_{g,r} = 0.02$ $S_{a,r} = 0.25$	*n = 3.0* $S_{g,r} = 0.01$ $S_{a,r} = 0.06$
Kinetic reaction parameters		
Activation energy E	8.1×10^{4} J/mol	*N/C*
Intrinsic rate constant K_0	3.6×10^{4} kg m^{-2} Pa^{-1} s^{-1}	*N/C*
Area Factor F_A	1.0	*N/C*

[1] *N/A* indicates parameter is not applicable; *N/C* indicates no change from previous value.
[2] See [19] and [5] for details.
[3] Brooks-Corey Model [20], modified to account for effect of hydrate on capillary pressure; G is the error function that smoothes curve near S^*=0; Bx is the incomplete beta function with parameters a and b [5].
[4] The effects of emerging fluid and solid phases on permeability are accounted for using the first Evolving Porous Medium (EPM) model of [5]. The permeability calculated with this model is also used to scale pressure [21].

References

[1] Sloan ED. Clathrate Hydrates of Natural Gases, New York: Marcel Dekker, Inc.; 1998.

[2] Milkov, AV. Global estimates of hydrate-bound gas in marine sediments: how much is really out there? Earth Sci Rev 2004; 66(3-4):183-97.

[3] Klauda JB, Sandler SI (2005), Global Distribution of Methane Hydrate in Ocean Sediment. Energy and Fuels 2005; 19:469-70.

[4] Moridis GJ. Numerical Studies of Gas Production from Methane Hydrates. SPE Journal 2003; 32(8):359-70.

[5] Moridis GJ, Kowalsky MB, Pruess K. TOUGH-Fx/Hydrate: A code for the simulation of system behavior in hydrate-bearing geologic media. Report LBNL/PUB 3185, Lawrence Berkeley National Laboratory, Berkeley, Calif.; 2005.

[6] Schmuck EA, Paull CK. Evidence for Gas Accumulation Associated with Diapirism and Gas Hydrates at the Head of the Cape Fear Slide. Geo-Marine Letters 1993; 13:145.

[7] Paull CK, Buelow WJ, Ussler W, Borowski WS. Increased Continental Margin Slumping Frequency During Sea-Level Low Stands Above Gas Hydrate-Bearing Sediments. Geology 1996; 24:143.

[8] Moridis GJ, Kowalsky MB. Response of oceanic hydrate-bearing sediments to thermal stress. Proceedings in Offshore Technology Conference, Houston, May, 2006.

[9] Kennett JP., Cannariato KG, Hendy IL, Behl RJ. Carbon isotope evidence for methane hydrate instability during late quaternary interstadials. Science 2000; 288: 128-133.

[10] Behl RJ, Kennett JP, Cannariato KG, and Hendy IL. Methane hydrates and climate change; the clathrate gun hypothesis. AAPG Bulletin 2003; 87(10):1693.

[11] Makogen YF. Hydrates of natural gas; 1974.

[12] Kim HC, Bishnoi PR, Heideman RA, Rizvi SSH. Kinetics of methane hydrate decomposition. Chem Eng Sci 1987; 42(7):1645-1653.

[13] Clark M, Bishnoi PR. Determination of activation energy and intrinsic rate constant of methane gas hydrate decomposition. Canadian Journal of Chemical Engineering 2001; 79(1):143-147.

[14] Moridis GJ, Seol Y, Kneafsey TJ. Studies of reaction kinetics of methane hydrate dissocation in porous media, Proceedings of the Fifth International Conference on Gas Hydrates, Trondheim, Norway, June 13-16; 2005.

[15] Moridis GJ, Collett T. Gas Production from Class 1 Hydrate Accumulations, in: Taylor C, Qwan J, Editors. Recent Advances in the Study of Gas Hydrates, Kluwer Academic/Plenum; 2004, p. 75-88.

[16] Moridis GJ, Kowalsky MB, Pruess K. Depressurization-induced production from Class-1 Hydrate Deposits, submitted to SPE Journal in 2005.

[17] van Genuchten M Th. A Closed-Form Equation for Predicting the Hydraulic Conductivity of Unsaturated Soils, Soil Sci Soc 1980; 44:892.

[18] Leverett, MC. Capillary Behavior in Porous Solids, Trans Soc Pet Eng AIME 1941; 142:152-169.

[19] van Genuchten M Th. A Closed-Form Equation for Predicting the Hydraulic Conductivity of Unsaturated Soils, Soil Sci Soc 1980; 44:892.

[20] Corey AT. The interrelation between gas and oil relative permeabilities. Producers Monthly 1954; November, p. 38-41.

[21] Leverett MC. Capillary Behavior in Porous Solids, Trans Soc Pet Eng AIME 1941; 142:152-169.